

Hou, Lixun  
Wang, Qingcai



<http://dx.doi.org/10.21278/brod73405>

ISSN 0007-215X  
eISSN 1845-5859

## INVESTIGATION ABOUT THE HYDRODYNAMIC COUPLING CHARACTERISTICS OF CONTRA-ROTATING AZIMUTH PROPULSOR

UDC 629.5.035.58:532.527

Original scientific paper

### Summary

A numerical study is conducted to determine the hydrodynamic coupling characteristics of a contra-rotating azimuth propulsor (CRAP) in open-water conditions. The detached-eddy simulation (DES) method is utilized to run simulations. A grid verification is conducted and the numerical results are validated based on a puller-type podded propeller. The hydrodynamic forces (i.e., thrusts and torques) are in accordance with the experimental data. The validated numerical method is utilized for subsequent CRAP simulations. The hydrodynamic performance and hydrodynamic coupling characteristics of CRAP are quantitatively analyzed according to forward propeller (FP), rear propeller (RP), and pod unit (PU) indicators with special focus on the hydrodynamic forces and the corresponding unsteadiness. PU appears to have essentially the same effect on the hydrodynamic performance of FP and RP. RP has a weak effect on the hydrodynamic performance of FP, while FP intensely affects that of RP. In general, the CRAP unsteadiness is dominated by RP, especially under heavy loading conditions.

*Key words: CRAP; Detached eddy simulation; Hydrodynamic performance; Unsteadiness; Vortex structure*

### Nomenclature

$\rho$	water density	$K_{TF} = \frac{T_F}{\rho n^2 D_F^4}$	thrust coefficient of the FP
$V_0$	inflow velocity		
$D_F$	diameter of the FP	$K_{TR} = \frac{T_R}{\rho n^2 D_F^4}$	thrust coefficient of the RP
$D_R$	diameter of the RP		
$n$	rotational speed	$K_{QF} = \frac{Q_F}{\rho n^2 D_F^5}$	torque coefficient of the FP
$Q_F$	torque of the FP	$K_{QR} = \frac{Q_R}{\rho n^2 D_F^5}$	torque coefficient of the RP
$Q_R$	torque of the RP		
$T_F$	thrust of the FP	$K_{RP} = \frac{-R_{pod}}{\rho n^2 D_F^4}$	resistance coefficient of the PU
$T_R$	thrust of the RP		

$R_{Pod}$	resistance of the PU	$J = \frac{V_0}{n D_F}$	advance coefficient
-----------	----------------------	-------------------------	---------------------

## 1. Introduction

As a combined propulsor, the contra-rotating azimuth propulsor (CRAP) has wide applications for its perfect energy-saving performance [1].

Authors of the present study have previously established a numerical procedure for CRAP design and energy-saving performance analysis based on lifting-line theory, lifting-surface theory and the low-order potential-based panel method. The designed CRAP showed an approximately 8% decrease in delivered power as compared with a conventional propeller under the same thrust conditions [2]. The CRAP showed the lowest delivered power when FP and RP were assigned optimal matching rotational speeds, and further, the energy-saving level decreased as inflow velocity increased [3]. These calculations were confined to the potential flow method, which can be operated quickly at low cost. The potential flow method is sufficient for the design and optimization of CRAPs as per hydrodynamic force predictions. However, its reliability is dubious in terms of its ability to predict the actual wake, reproduce unsteady vortex-wake interactions, and reproduce the unsteady vortex separation of the propellers and PU of CRAPs. Su et al. [4] predicted the hydrodynamic performance of CRAP through a BEM/RANS interactive method. The forward propeller and the aft propeller are handled by two separate BEM models while the interaction between them are achieved via coupling them with a RANS solver. The results are shown to be in good agreement with the experimental data. Currently, computational fluid dynamics (CFD) methods are commonly used as they can exploit modern computing power to accurately simulate viscous effects and hydrodynamic performance in marine propulsors over a wide range of inflow conditions [5]. CFD simulations were conducted at model scale in the present study to investigate the hydrodynamic characteristics of a CRAP and the mutual interactions among its different components.

The physical nature and evolutionary mechanism of the propeller wake are directly related to the hydrodynamic performance. Therefore, these indicators can be used to accurately predict the propeller performance [6]. Many high-resolution simulations of the turbulent field generated by marine propulsors have been conducted in recent years. The large-eddy simulation (LES) methods can be effectively used for vorticity field simulation and instability prediction in the wake [7]. Kumar and Mahesh [8] conducted wake simulation of a propeller via LES, then explored the axial evolution of the propeller wake in detail. Although the mutual-inductance mode dominates the propeller instability, the actual mechanism depends on the propeller geometry and operating conditions. Once the propeller wake became unstable, the coherent vortical structures broke apart and evolved into the far wake. Posa et al. [9] investigated submarine propeller in open-water conditions using LES. The rotating geometry of the propeller within a stationary cylindrical grid was handled by an immersed boundary approach. Direct comparisons with particle image velocimetry (PIV) experiments demonstrated that such simulations accurately reproduced wake characteristics. Heydari and Sadat-Hosseini [10] conducted CFD simulations to study the wake field behind a marine propeller under open-water conditions. The local variables and the wake structure characteristics were analyzed to determine integral variables and their correlations with the variables.

The detached-eddy simulation (DES) combines the features of the RANS method in the near-wall region and LES in other regions to comprehensively describe the flow features over a wide spectrum of applications, ranging from simple propeller analyses at both model and

full scales to self-propulsion in waves [11-14]. Di Mascio et al. [15] investigated the hydrodynamic performance of a propeller under oblique flow conditions using DES to find a very complex vortical system composed of a strong tip vortex, less intense trailing vortices under loading variation, different blade root vortices, and an intense hub vortex. Gong et al. [16] conducted a comparative DES analysis on the evolution of wake vortices generated by ducted and non-ducted propellers, and their spatial evolution mechanisms under various loading conditions. Lungu [17] investigated the hydrodynamic performance of a five-bladed controllable pitch propeller in open water via DES by comparison against experimental data. Sun et al. [18] simulated the effects of the scale on propeller wake evolution in open water using the DES method. They found that scale does affect the load and wake dynamics of the propeller under different conditions. For a combined propulsor, accurate simulations about the mutual interactions among different components of the propulsor are the key to the performance predictions. The numerical methods have been successfully applied to reveal the mutual interaction mechanism among different components, and the performances of combined propulsors in hydrodynamics [19, 20] or aerodynamics [21, 22] were simulated accurately. On the hydrodynamics side, Zhang et al. [19] studied the interaction between the forward and aft propellers in a pod propulsion system with a set of hybrid CRPs with a focus on the global quantities and the flow details using the DES method. The results were in satisfactory agreement with the corresponding model test data. Hu et al. [20] applied the DES method to hydrodynamic performance simulations of CRPs successfully, and the results were used for cavitation noise predictions in further. However, the correlational researches did not focus on the unsteady characteristics of propulsors. Considering that the unsteadiness of propulsor's hydrodynamic forces is a key factor of noise and fluctuating pressure, it's of great significance to have a deep insight into the hydrodynamic coupling characteristics and unsteadiness of propulsors.

The aim of this study is to investigate the hydrodynamic coupling interactions among the FP, RP, and PU of a CRAP in open-water conditions. Simulations are conducted in the commercial CFD solver STAR-CCM+. There are strong interactions among the wake vortices of FP, RP, and PU, such interactions as well as the corresponding flow features can be accurately reflected in DES results. A grid verification is conducted to evaluate the numerical uncertainties and the results are validated by comparison against experimental data for a puller-type podded propeller. The hydrodynamic coupling characteristics of CRAP are analyzed based on the FP, RP, and PU, respectively. The results reveal the mutual coupling interactions of the hydrodynamic forces and corresponding unsteady characteristics among FP, RP, and PU. This work may provide workable technical support for the optimal design and application of CRAPs.

## 2. Verification and validation studies

### 2.1 Geometric model and mesh generation

The numerical method used in this study is validated based on the experimental data for a given puller-type podded propeller. Table 1 shows the main parameters of the podded propeller modified from the DTMB P4119 propeller, and the specific geometry information of the podded propeller can be referred to the work by Liu et al. [23]. Fig. 1 shows the geometry of the podded propeller and the corresponding coordinate systems, which includes the propeller-fixed local coordinate system  $o-xyz$  and the global coordinate system  $O-XYZ$ . The origins of these two coordinate systems coincide at the propeller disk center. For the global coordinate system  $O-XYZ$ , the Y-axis is positive to starboard, the Z-axis is positive in the vertically upward direction, and the X-axis coincides with the propeller axis pointing to the

downstream. The local coordinate system  $o-xyz$  rotates along with the propeller with the  $y$ -axis coinciding with the reference line of the key blade, and the  $x$ -axis coinciding with the  $X$ -axis. The  $z$ -axis is determined by the right-hand rule.

**Table 1** Main parameters of the puller-type podded propeller

Parameter	Value
Propeller diameter, $D$ (m)	0.27
Number of blades	4
Hub ratio	0.26
Blade pitch distribution(constant)	$P/D=1.0$
Pod diameter (m)	0.139
Pod length (m)	0.41
Strut height (m)	0.30
Strut chord length (m)	0.225

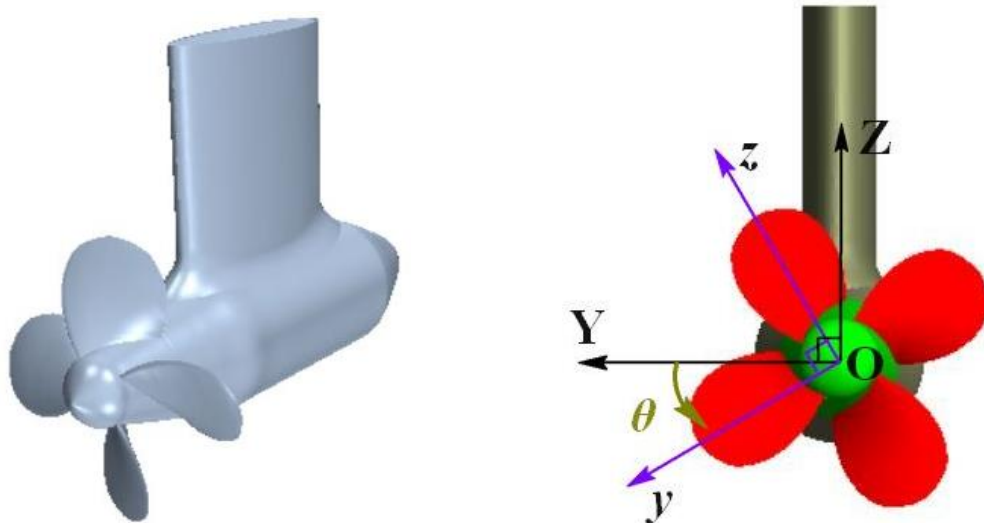


**Fig. 1** Geometrical model of the puller-type podded propeller

Fig. 2 shows the boundary conditions of the computational domain, which extended  $5D$  upstream and  $15D$  downstream from the propeller disk center. The top, bottom, and side boundaries are  $5D$  from the propeller shaft. The inlet boundary is set as the velocity inlet. The top, bottom, and side boundaries are set as the symmetry condition. The outlet boundary is set as the pressure outlet. The propeller rotation is handled via sliding grids. This generates one rotating subdomain which encloses the propeller. The surfaces of the blade, hub, and PU are set as no-slip walls.

The trimmed cell method is adopted to generate the hexahedral mesh. Fig. 3 shows the cross-sections of the computational mesh for the puller-type podded propeller simulations in the  $X$ - $Y$  and  $Y$ - $Z$  planes. The entire computational domain is divided into three subdomains: The rotation domain, a cylinder with a diameter of 1.3 times that of the propeller contains the rotating propeller as well as the hub; The slipstream domain, the area downstream of the propeller; The background domain, the remainder of the full computational domain. Technically, the slipstream domain is a part of the background domain. The sliding mesh method is adopted for the propeller rotation simulation.

The contacting surface between the rotation domain and static domain is set as an interface to enable the exchange and the iteration of information. Grid refinement is applied to

the rotational domain around the propeller to have sufficient flow field resolution. Smaller grid spacing is applied to the blade edges and the intersects between the blades and hub. Eight layers of prism mesh are distributed around the wall surfaces to effectively capture the boundary flow [24]. The boundary layer thickness increases progressively in geometric progression with a ratio of 1.2. The SST  $k-\omega$  DES model which combines the features of the SST  $k-\omega$  RANS model in the boundary layers with the LES model in other regions is adopted to simulate the flow field [25]. The first-layer thickness of the boundary layer is restricted to  $y^+ < 1$  to satisfy the requirement of the DES method for different inflow conditions. A refined mesh in the slipstream domain is generated to capture the formation and evolution of the propeller vortex structure.

For the specific numerical simulations, the transport equations of the SST  $k-\omega$  turbulence model are computed using the second-order upwind and central difference schemes. The coupling of the pressure and velocity is solved using the SIMPLE method. A second-order convection scheme is used for the momentum equations. A second-order implicit scheme is used for temporal discretization and five inner iterations per time step were used. The sliding mesh method is used to simulate propeller rotation. The all- $y^+$  wall treatment is used to predict the flow and turbulence parameters across the wall boundary layer.

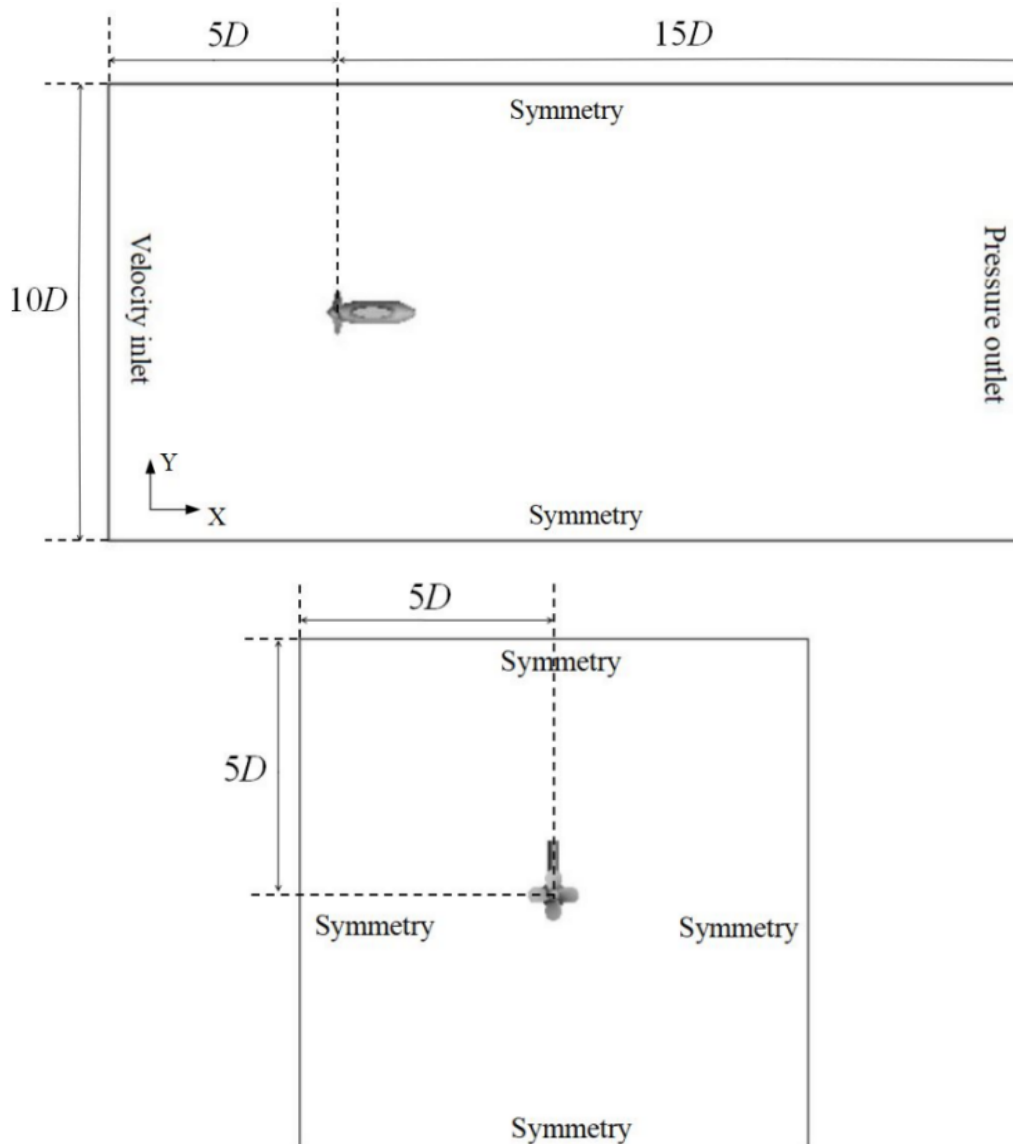
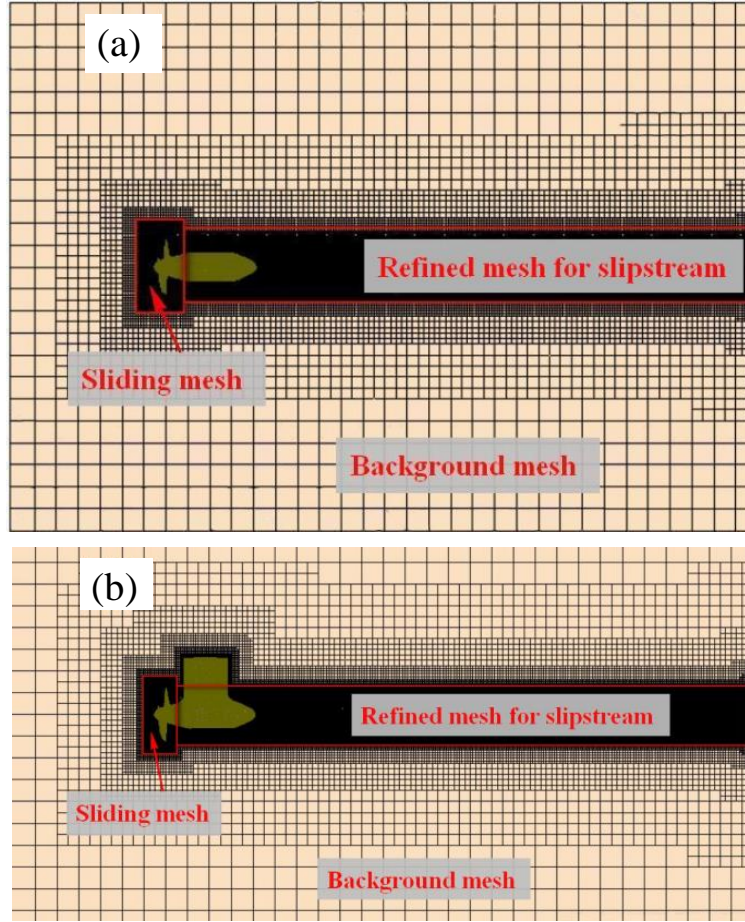


Fig. 2 Computational domain and boundary conditions.



**Fig. 3** Cross-sections of computational mesh for puller-type podded propeller in (a) X-Y plane and (b) Y-Z plane

## 2.2 Grid sensitivity analysis

The grid sensitivity is assessed using the two-grid assessment procedure [26] which needs less computation burden compared with the three-grid method [27]. This method has been effectively applied for propeller DES simulations [28] and podded propulsors [19]. A refined grid is generated by decreasing the grid size with the refinement factor of  $\sqrt{2}$  globally based on the basic grid. Adjusting the grid size of the basic grid dynamically until the results do not change significantly with a finer grid. The time steps for different cases are determined under the condition that the  $CFL$  is below 1.0.

Table 2 gives the final results of the grid sensitivity analysis. The basic and the refined grids have  $9.1 \times 10^6$  and  $25.7 \times 10^6$  grids respectively.  $K_T$  and  $K_Q$  are the non-dimensional thrust and torque coefficients.  $f_1$  and  $f_2$  represent the results of the refined grid and the basic grid.  $f_0$  denotes the experimental data given by Liu et al [29],  $(f_0 - f_2) \% f_0$  denotes the basic grid error, and  $(f_0 - f_1) \% f_0$  is the refined grid error.  $E$  is the error of the refined grid and is defined as  $E = \frac{f_2 - f_1}{1 - r^p}$  ( $r$  is refinement factor,  $p$  is the formal order of accuracy of the algorithm and is set as 2 as suggested by Roache [26] in this work).  $U_N$  is the uncertainty and is calculated as  $U_N = F_s |E|$  ( $F_s$  is the safety factor depending on the number of grids used, and the value of 3 is adopted when only two grids are used according to Roache [26]).

Five advance coefficients, namely  $J=0.2, 0.4, 0.6, 0.8$  and  $1.0$ , are considered. The rotational speed is kept 15 rps and  $J$  is adjusted through changing the inflow velocity. The thrust and torque coefficients given in Table 2 are the averages over four propeller revolutions

under convergence condition considering the unsteadiness caused by the interactions between PU and propeller. The  $U_N$  values for the hydrodynamic forces under different inflow conditions are very small, and the hydrodynamic force differences between the basic grid and the refined grid for different inflow conditions are less than 0.96%. what's more, the basic grid results show a good agreement with the experimental data with the calculation errors being less than 2.85%.

**Table 2** Grid sensitivity analysis

	Exp.	Basic		Refined		$(f_1 - f_2)\% f_1$	$E$	$U_N\% f_1$
		Cal.	$(f_0 - f_2)\% f_0$	Cal.	$(f_0 - f_1)\% f_0$			
$J=0.2$								
$K_T$	0.421	0.409	2.85	0.412	2.14	0.73	$3.0 \times 10^{-3}$	2.18
$10K_Q$	0.602	0.589	2.15	0.592	1.66	0.51	$3.2 \times 10^{-3}$	1.62
$J=0.4$								
$K_T$	0.345	0.337	2.32	0.339	1.74	0.59	$2.2 \times 10^{-3}$	1.9
$10K_Q$	0.526	0.514	2.28	0.519	1.33	0.96	$4.5 \times 10^{-3}$	2.6
$J=0.6$								
$K_T$	0.254	0.248	2.36	0.249	1.97	0.40	$8.5 \times 10^{-4}$	1.0
$10K_Q$	0.417	0.409	1.92	0.412	1.20	0.73	$3.1 \times 10^{-3}$	2.2
$J=0.8$								
$K_T$	0.159	0.156	2.02	0.157	1.45	0.64	$9.0 \times 10^{-4}$	1.7
$10K_Q$	0.294	0.288	1.89	0.290	1.36	0.69	$1.5 \times 10^{-3}$	1.6
$J=1.0$								
$K_T$	0.064	0.062	2.81	0.063	1.88	0.96	$6.0 \times 10^{-4}$	2.86
$10K_Q$	0.174	0.170	2.29	0.171	1.72	0.58	$1.0 \times 10^{-3}$	1.75

The trailing vortex structures are simulated using the basic grid under different inflow conditions to determine whether the grid density captures the formation and evolution of the vortex structure [30]. Considering that the threshold on  $Q$  factor for fully developed trailing vortex decreases with the increase of inflow velocity, Fig. 4 gives the iso-surfaces of different  $Q$  values,  $Q$  is set to 2000, 1500, and 1000 for  $J=0.4, 0.6,$  and  $0.8,$  respectively. The iso-surfaces of  $Q$  are colored by the local velocity magnitude. The vortex structure of the podded propeller mainly consists of the tip vortex and hub vortex, and the vortex systems are well-developed. The tip vortices deform obviously after colliding with the leading edge of the strut, and this trend gets more obvious with the decrease of inflow velocity. The vortex pairing appears in Figs. 4(a) and 4(b), and is more obvious in Fig. 4(a) by comparison.

In general, the basic grid strategy appears to not only perform well in terms of accuracy but also in capturing the vortex structure formation and evolution. The refined grid cases have higher accuracy but bear great computation burden. Therefore, the basic grid strategy is adopted for the following simulations.

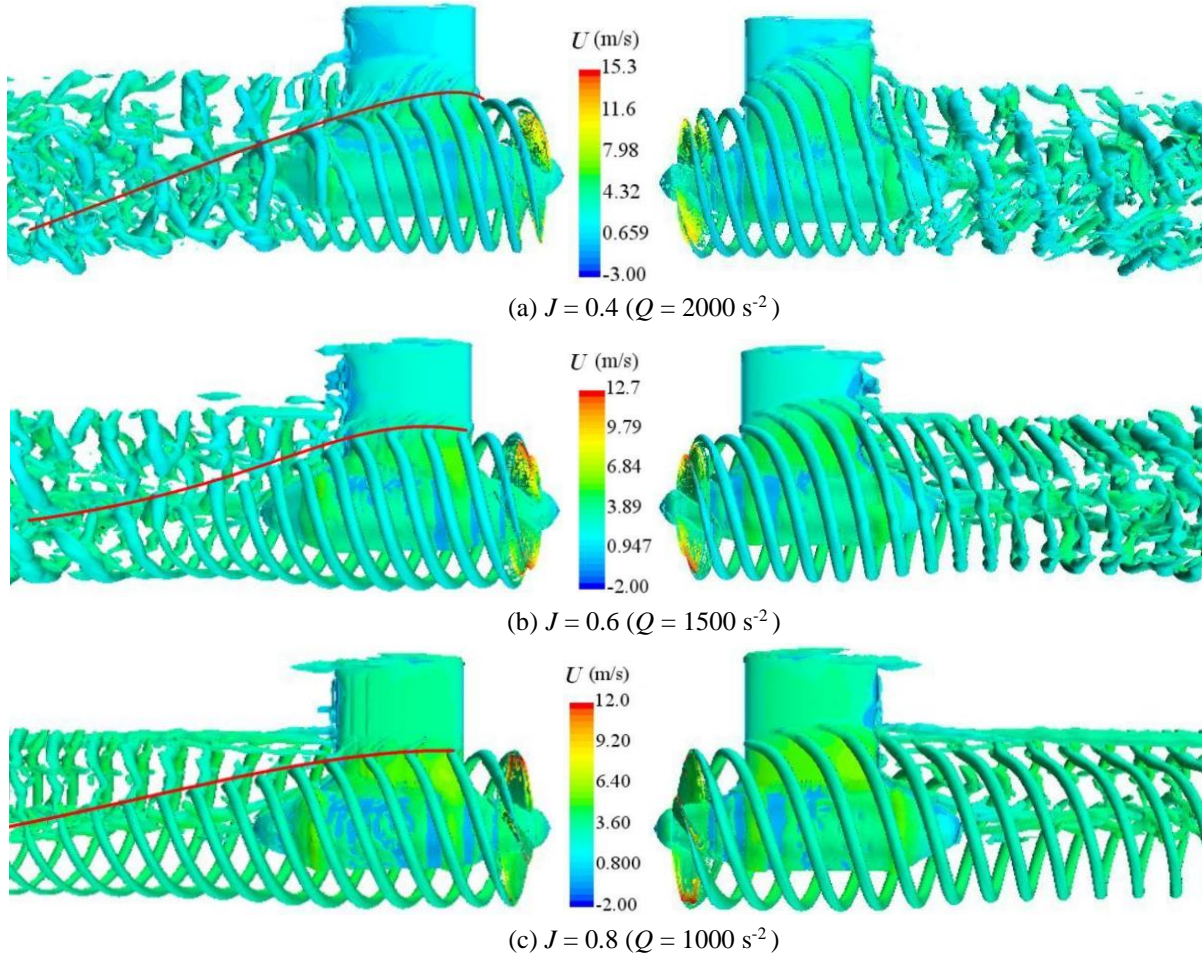


Fig. 4 Vortex structures of the puller-type podded propeller under different inflow conditions (basic grid)

### 3. Simulation results

The open-water hydrodynamic performance of the CRAP designed by Hou et al. [2] are further investigated in this study. The hydrodynamic indicators of the FP, RP and PU are respectively analyzed to quantitatively observe the hydrodynamic performances and coupling mechanism of the CRAP.

#### 3.1 Geometry description

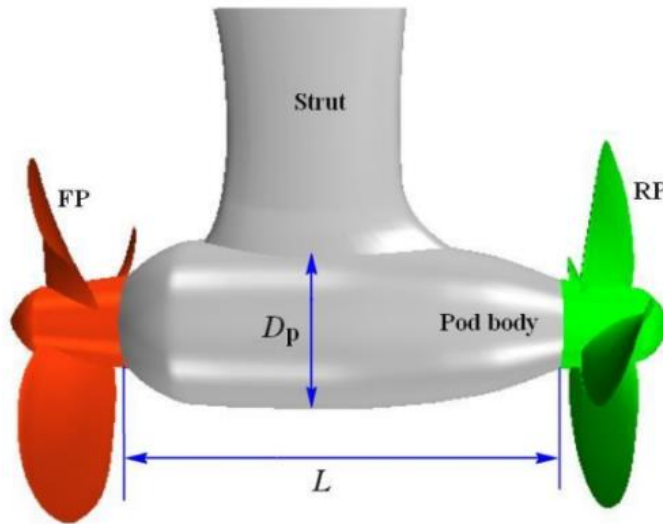
Table 3 lists the main parameters of PU, where the length  $L$  and diameter  $D_p$  of the pod body are as defined in Fig. 5. A symmetrical NACA0012 airfoil is adopted for the strut. The main parameters of FP and RP are given in Table 4. A modified NACA66 section with  $a = 0.8$  is adopted for both FP and RP. The propellers are both assigned a skew of  $12^\circ$  and a rear rake of  $15^\circ$ . FP and RP are set to rotate in opposite directions.

Table 3 Main parameters of PU.

Parameter	Value
Pod diameter $D_p$ (m)	0.103
Pod length $L$ (m)	0.256
Strut height (m)	0.156
Strut average chord length (m)	0.116
Strut width (m)	0.016

**Table 4** Main parameters of FP and RP.

Parameter	FP	RP
Diameter (m)	0.25	0.2275
Number of blades	3	4
Pitch ratio of 0.7R	0.97	1.25
Chord length of 0.7R (m)	0.086	0.067
Blade thickness at blade root (m)	0.0087	0.0078
Camber value of 0.7R (m)	0.0023	0.0021
Disc ratio	0.41	0.50
Direction of rotation	Right-handed	Left-handed



**Fig. 5** Geometric parameters of pod body

Similar to the puller-type podded propeller discussed in Section 2, the coordinate system utilized in this analysis includes global reference and local frames, as shown in Fig. 6. Unlike the global reference frame of the puller-type podded propeller, the origin of the global reference frame  $O\text{-}XYZ$  of CRAP is located at the intersection of the propeller axis and the vertical axis of the strut shaft. The local frames  $o\text{-}x_F y_F z_F$  and  $o\text{-}x_R y_R z_R$  of FP and RP are defined accordingly. The axis directions of the coordinate system have the same definitions as that in Section 3. The basic grid strategy (Section 3) is used in these simulations as well, so the grid number is different for cases targeting various geometric configurations. FP and RP have the same rotational speed  $n=10$  rps in all simulation cases.

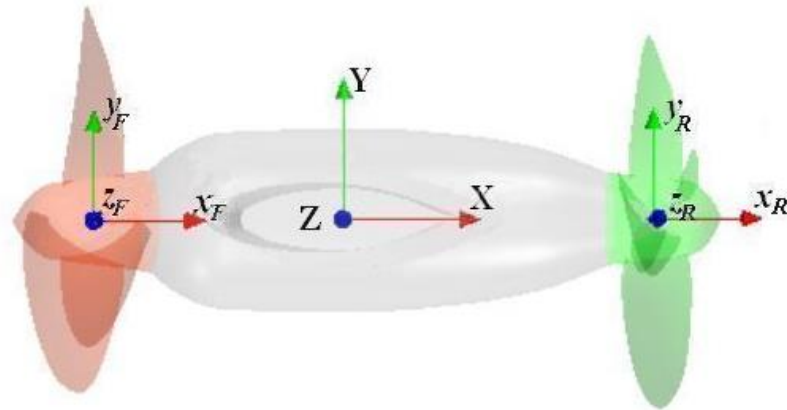


**Fig. 6** Coordinate system of the CRAP

### 3.2 Hydrodynamic performance analysis of FP

The hydrodynamic coupling mechanism among FP, RP, and PU is investigated from FP perspective first. To reveal the effects of PU and RP on the hydrodynamic characteristics of FP, the hydrodynamic indicators of FP alone, FP+PU, and CRAP at various advance coefficients ranging from 0.1 to 1.0 are simulated. The vortex structures and tangential velocities in the wake field are also analyzed in detail. For FP simulations, the end of the hub is closed using a semi-elliptical sphere with a major axis length of 1.2 times the minor axis length, which is equal to the diameter of the end of the FP hub. For FP+PU cases, the hub of RP is included to close the geometry. Fig. 7 shows the geometries of FP alone and FP+PU. Fig. 8 and Fig. 9 show the computational meshes for CRAP, FP+PU and FP alone used for simulations.

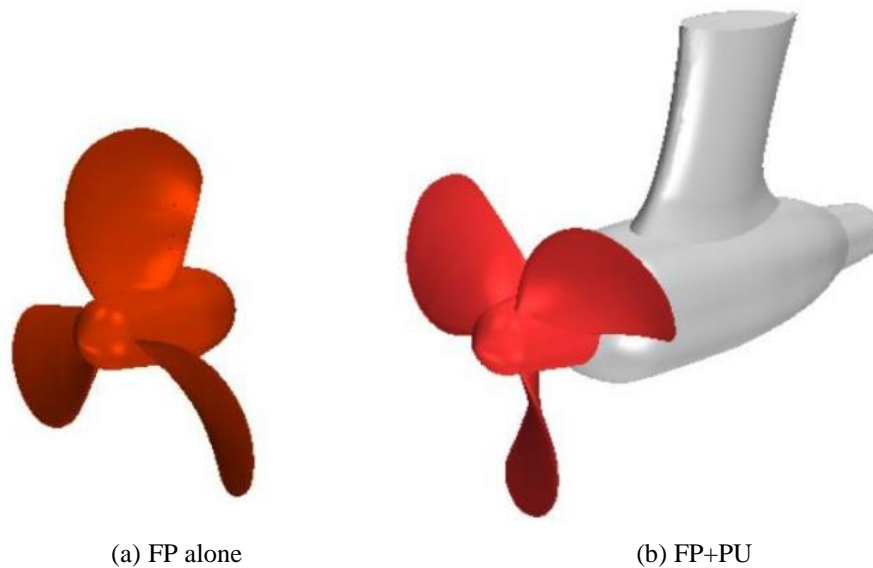


**Fig. 7** Geometries used for FP analysis

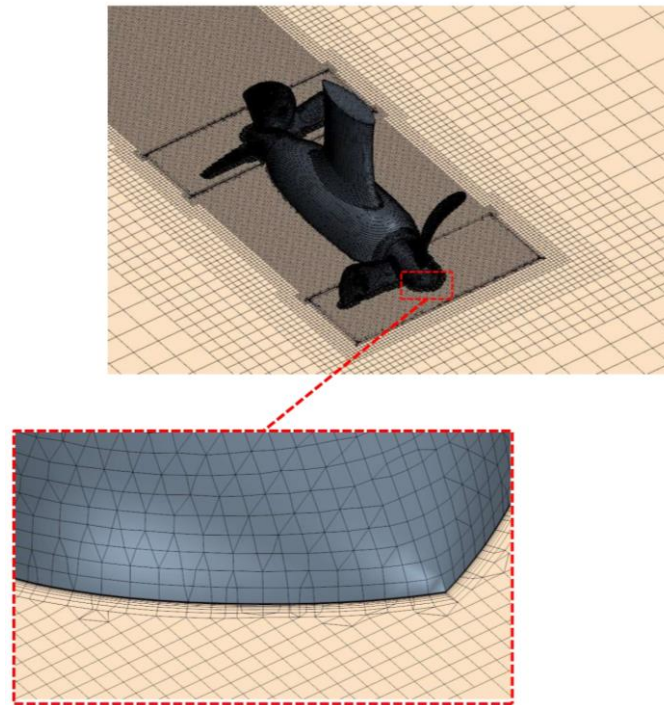
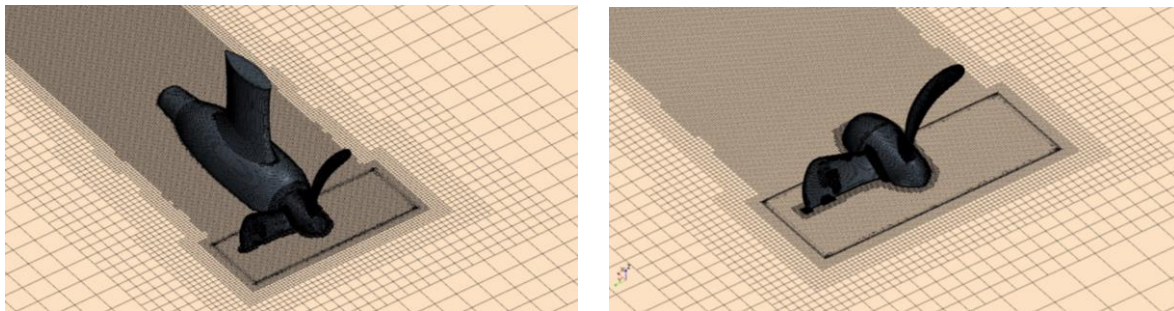


**Fig. 8** Computational mesh for CRAP and boundary layer



(a) FP + PU

(b) FP alone

**Fig. 9** Computational meshes for FP + PU and FP alone

Fig. 10 shows the trailing vortex structures visualized by iso-surfaces of  $Q$  at  $J=0.4, 0.6,$  and  $0.8$  for the FP alone, FP+PU, and CRAP cases with the phase angles (denoted by  $\theta$ ) of FP and RP being  $0^\circ$ . For visual clarity,  $Q$  is set to 1200, 700, and 200 for  $J=0.4, 0.6,$  and  $0.8,$  respectively; the vortex structures are colored by the local velocity magnitude. The vortex systems of the FP alone, FP+PU, and CRAP are well-developed. With respect to FP alone (Figs. 10(a1)-(c1)), on the whole, the vortices have regular shapes and the trajectories of the tip vortices generated by different blades are clearly helical without external disturbance. A vortex-pairing phenomenon is observed approximately  $2D_F$  downstream of the propeller at  $J=0.4$ , as shown in Fig. 10(a1). The vortices become stronger and the self- and mutual induction between adjacent tip vortices intensify as advance coefficient decreases. Moreover, the distance between neighboring tip vortices is small under heavy loading conditions. These situations result in the early onset of merging and grouping during the evolution of the tip vortices.

The existence of PU alters the wake vortex structure patterns to some extent, and this effect intensifies as the advance coefficient decreases (Figs. 10(a2)-(c2)). The strut destroys the stable structures of the FP vortices and is particularly destructive under heavy loading conditions. The tip vortices deform after colliding with the leading edge of the strut, then are split by the strut with opposite displacements on either side in the vertical direction. The

vortex pairing phenomenon occurs earlier as compared with the cases of the FP alone due to the effect of PU. With respect to CRAP, RP works in the slipstream of FP and PU. The tip vortices of FP and RP collide as the RP diameter is approximately equal to the transverse diameter of the contracted FP slipstream. This situation immediately triggers instability in the tip vortex structure and directly leads to the breakdown of the tip vortices, as shown in Figs. 10(a3)-(c3). This tip vortex instability is more obvious at lower advance coefficients, as the heavier loading condition strengthens the slipstream contraction and expands the overlapping region between FP and RP slipstreams. However, in the FP+PU configuration, the tip vortices maintain a regular helical trajectory without complete breakdown after colliding with the strut. Therefore, The tip vortex instability of CRAP is mainly caused by the intense interactions of FP and RP.

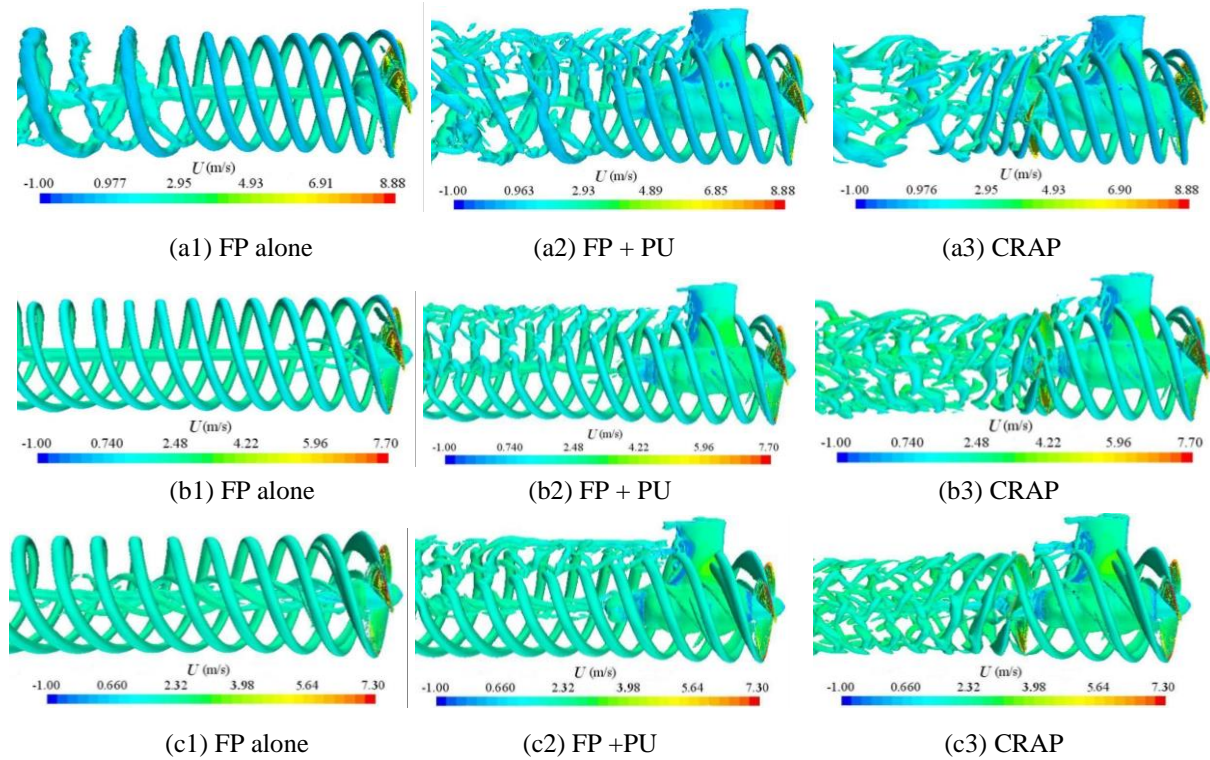
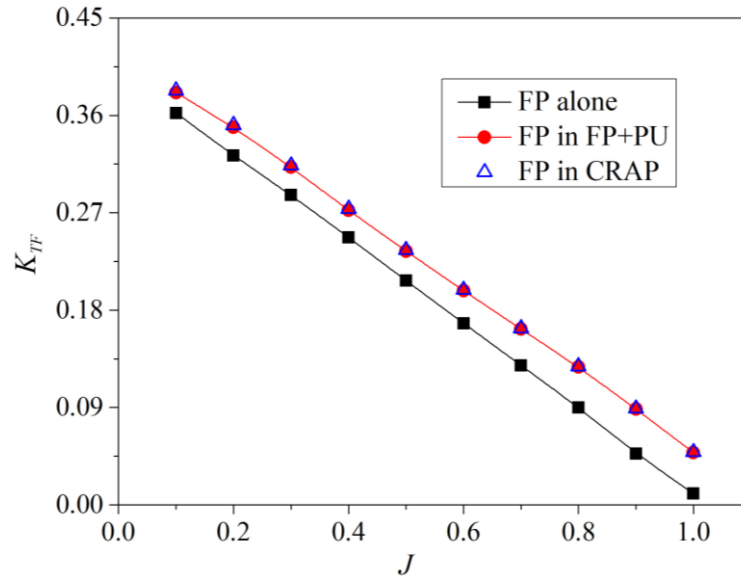


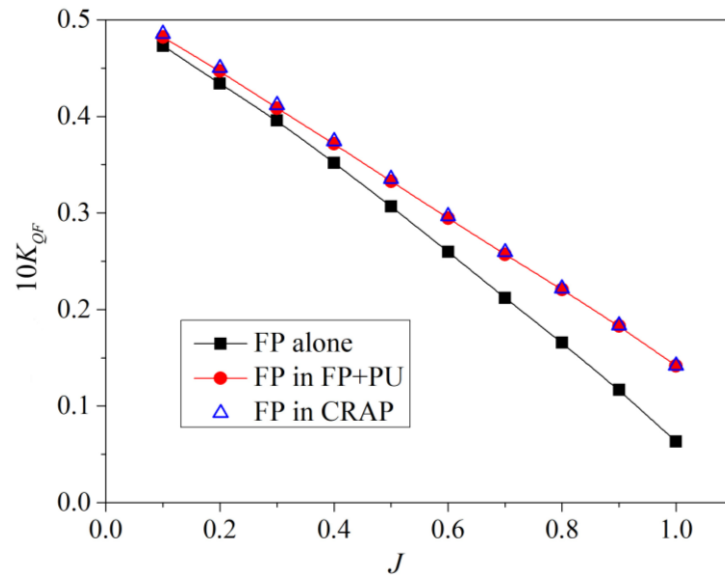
**Fig. 10** Vortex structures based on iso-surfaces of  $Q$  at  $\theta = 0^\circ$ . (a1-a3)  $J = 0.4$ ,  $Q = 1200$ ; (b1-b3)  $J = 0.6$ ,  $Q = 700$ ; (c1-c3):  $J = 0.8$ ,  $Q = 200$ .

The time-averaged hydrodynamic forces (thrusts and torques) of FP, over four revolutions under convergence condition, in three different configurations at various advance coefficients are displayed in Fig. 11. The FP thrusts and torques decrease as the advance coefficient increases. Overall, the hydrodynamic forces of the FP alone are lower than those of FP in FP+PU and CRAP. This phenomenon is mainly caused by the blockage effect of PU, which reduces the FP inflow velocity. The hydrodynamic forces of FP in CRAP are slightly higher than those of FP in FP+PU, but the differences are negligible. Thus, RP has little effect on the hydrodynamic forces of FP.

The changes in hydrodynamic forces of FP in FP+PU and CRAP compared with those of FP alone can be mainly attributed to the effect of PU. Compared with FP alone, the added values of FP thrusts in FP + PU and CRAP slightly increase as advance coefficient increases. In all, the effect of PU on FP thrust gets a little intensified with the increase of inflow velocity. However, the effect of PU on FP torque gets more remarkable under light loading conditions.



(a) Thrusts



(b) Torques

**Fig. 11** Time-averaged thrusts and torques of FP in three different configurations

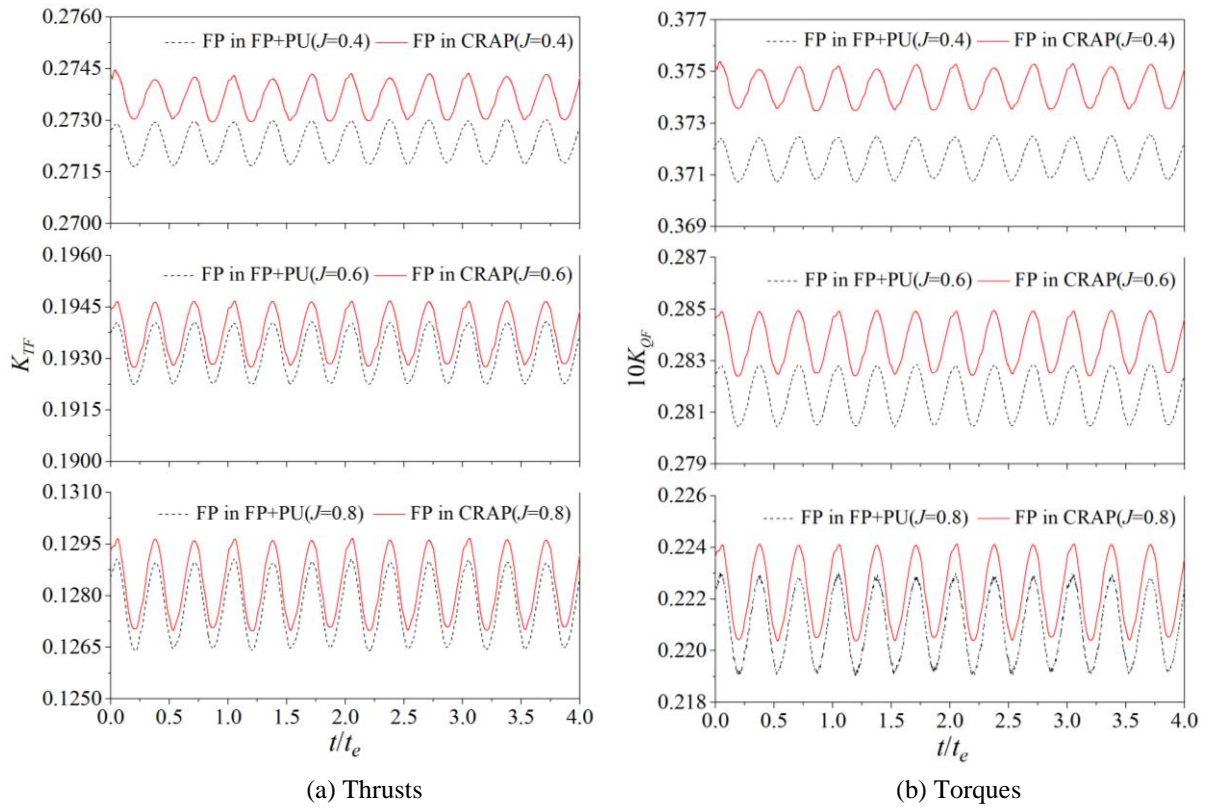


**Fig. 12** Hydrodynamic forces of FP in different configurations over four revolutions under convergence conditions

The hydrodynamic performances of a CRAP are simulated in a uniform flow field, but show some unsteadiness due to the interactions among FP, RP and PU. The fluctuating hydrodynamic forces are closely correlated with the fluctuating pressure and radiated noise, so the unsteady characteristics of CRAP hydrodynamic forces shall be known. The effects of PU and RP on the unsteady characteristics of FP hydrodynamic forces are discussed in this subsection.

The effects of PU and RP on the hydrodynamic forces of FP and the corresponding unsteadiness are observed. Fig. 12 gives the hydrodynamic forces of FP in FP+PU and CRAP over four revolutions under convergence conditions at the advance coefficients of  $J = 0.4, 0.6,$  and  $0.8$ . The variable  $t_e$  denotes the rotation period of propeller. The hydrodynamic forces of FP alone are not included in Fig. 12, as the motion of FP alone is steady and its hydrodynamic forces do not change over time.

Given the significant difference between the hub configuration of FP alone and those of FP in FP+PU and CRAP, the hydrodynamic forces given in Fig. 12 refer to the hydrodynamic forces of FP blades. The hydrodynamic forces of FP in CRAP change synchronously with those of FP in FP+PU. They also decrease as the advance coefficient increases and are slightly higher in CRAP than in FP+PU. The fluctuating amplitudes of thrusts and torques increase with the increase of advance coefficient, and the fluctuating amplitudes of the hydrodynamic forces of FP in CRAP are basically the same as those of FP in FP+PU. This means that the unsteadiness of the hydrodynamic forces of FP is mainly caused by PU, and that the effect of RP on the unsteadiness of the hydrodynamic forces of FP can be neglected.

Fig. 13 shows the unsteady change trends of the hydrodynamic forces of the key blade of FP in time domain. The hydrodynamic forces of the key blade of FP in CRAP are slightly greater than those of the key blade of FP in FP+PU, and the differences between them

decrease as advance coefficient increases. The key blade of FP is located at  $Y+$  at  $t/t_e = 0$ . Its hydrodynamic forces change periodically with similar fluctuating amplitudes in FP + PU and CRAP. The hydrodynamic forces of the key blade of FP have the maximum values at the position just in front of the strut and the minimum values at  $Y+$ . The unsteadiness of the hydrodynamic forces of the key blade of FP can thus be attributed to the up-down asymmetry of PU.

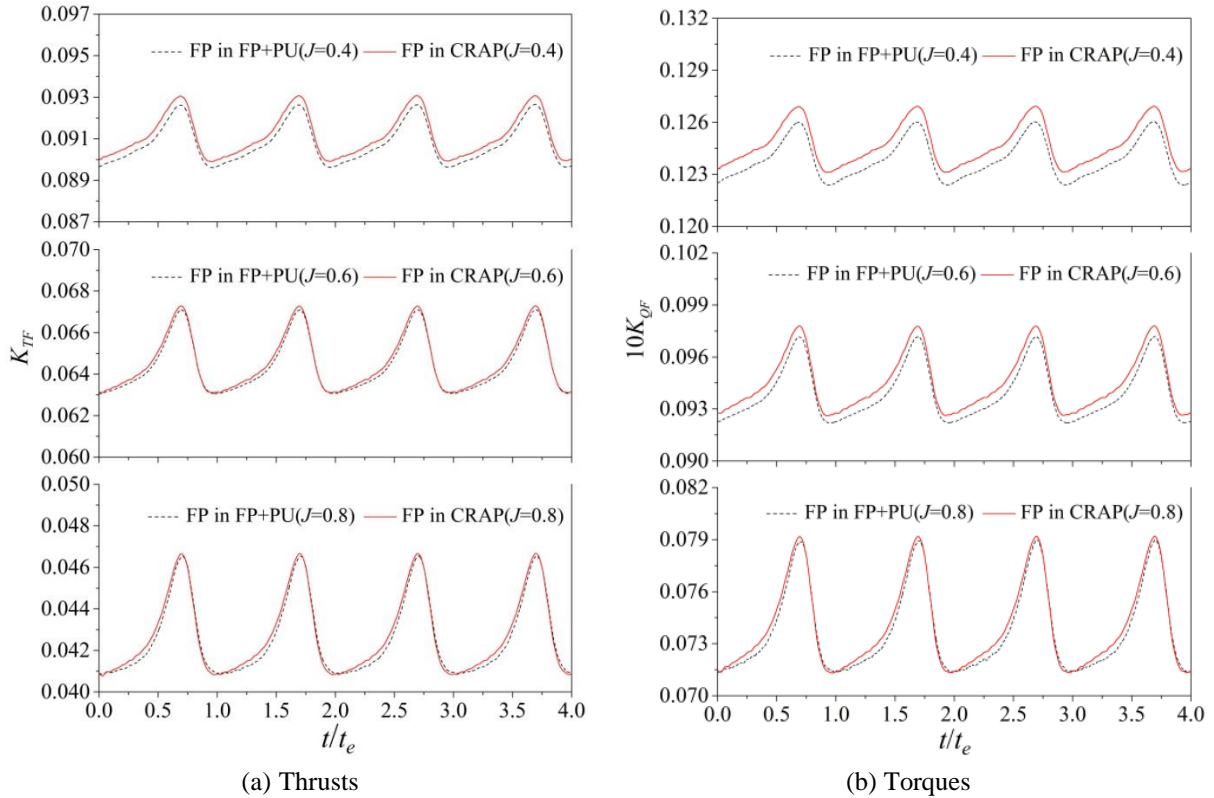


**Fig. 13** Hydrodynamic forces of the key blade of FP in different configurations over four revolutions under convergence conditions

The tangential velocity distributions at  $J=0.6$  and  $t/t_e = 0$  are compared at three transverse planes: Plane A, Plane B, and Plane C (Fig. 14). Plane A is located  $0.58D_F$  downstream of the FP disc, Plane B is  $1.16D_F$  downstream, and Plane C is  $2.0D_F$  downstream. Therefore, Plane A is located at the middle of the strut while Plane B is located just before RP.

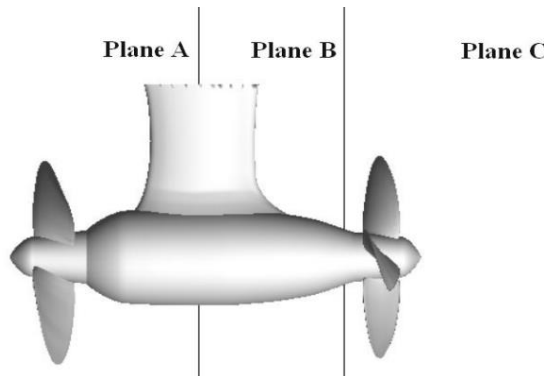


**Fig. 14** Planes used for comparisons of tangential velocity distributions

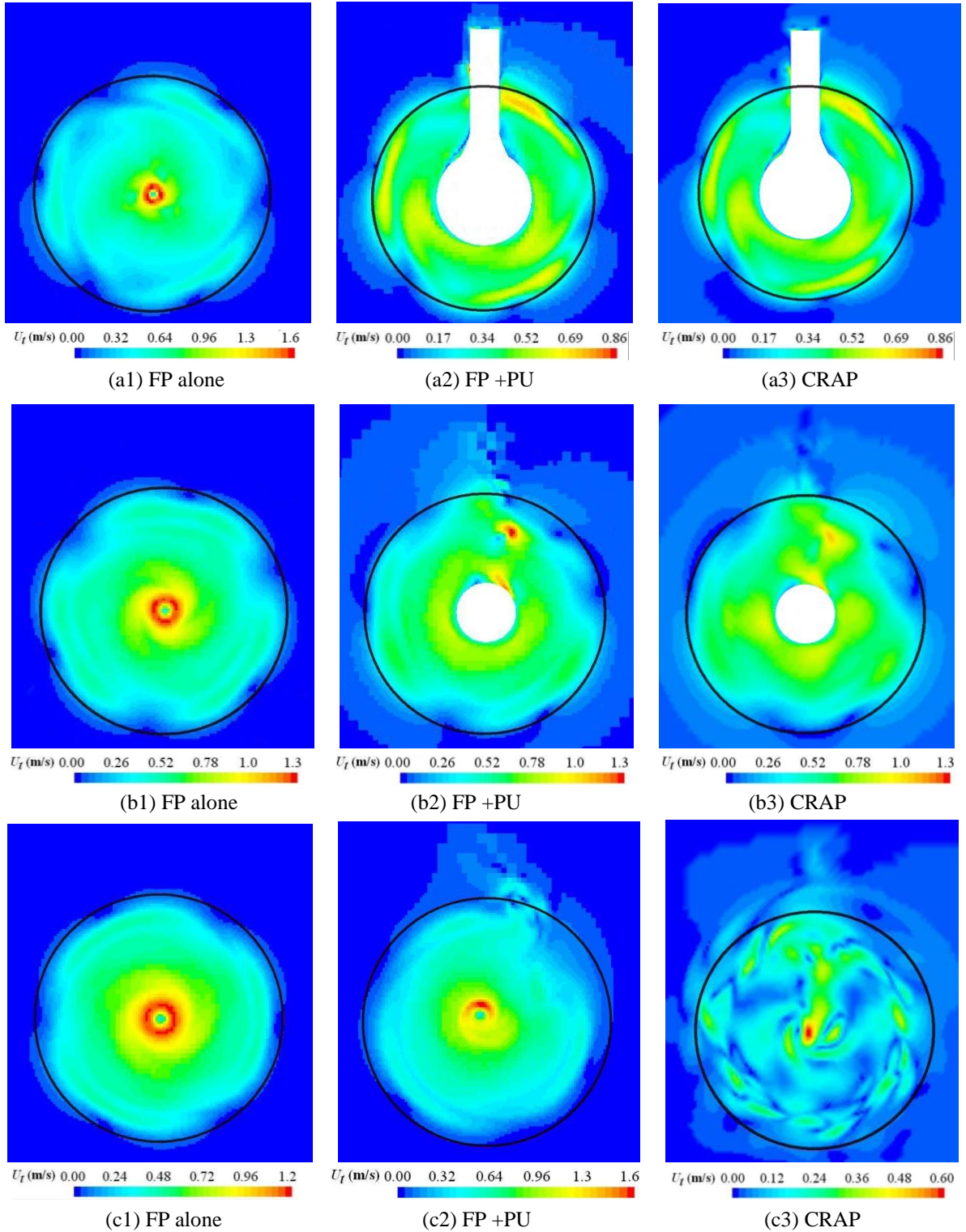


**Fig. 15** Tangential velocity distributions at different transverse planes at  $J = 0.6$  and  $t/t_e = 0$ : (a1)-(a3) Plane A; (b1)-(b3) Plane B; (c1)-(c3) Plane C

As shown in Fig. 15, the tangential velocity distributions of FP in three different configurations exhibit marked differences. With respect to FP alone, the tangential velocity distributions on different transverse planes present three of the same change cycles corresponding to the number of FP blades, especially for Plane A. The maximum tangential velocity occurs behind the hub owing to the rotational hub vortex (Fig. 10), then decreases slightly as it moves downstream. The tangential velocity distribution on the downstream plane

is more uniform compared to that on the upstream plane; this phenomenon intensifies in the area behind the hub. PU has an obvious effect on the tangential velocity distribution of FP in FP+PU. The maximum tangential velocity appears on the right side of the strut, as shown in Figs. 15(a2) and 15(b2). This is mainly because the FP slipstream deforms after colliding with the strut and is split by the strut with opposite displacements on two sides in the vertical direction. The FP slipstream at the port side has an upward movement, and that at the starboard has a downward movement. Considering the blockage effect of the strut and the rightward rotary motion of FP, the tangential velocities at the port side decrease to some extent. However, the nearby fluid floods into the starboard side to compensate for the local downward flow loss. Therefore, the tangential velocities at the starboard side are higher than those at the port side. The tangential velocities on Plane C have a concentrated area of high values due to the existence of PU. The mean tangential velocity on Plane C in FP+PU is slightly lower than that of FP alone. In general, the effect of PU on the tangential velocities of FP on Plane C is not obvious.

The tangential velocity distribution of FP in CRAP is similar to those of FP in FP+PU on Plane A and Plane B. Nevertheless, the values of tangential velocity of FP in CRAP are slightly smaller than those of the FP in FP+PU on Plane A and Plane B owing to the existence of RP. The difference is more obvious on Plane B as the Plane B is closer to RP. Overall, RP has weak effect on the flow filed upstream. However, the tangential velocity distribution on Plane C is much different from those of FP alone or FP+PU. The mean tangential velocity in CRAP on Plane C is remarkably lower than those in FP alone or FP+PU. To this effect, the rotational energy of FP in CRAP behind RP is effectively recovered. This result indicates that RP has a remarkable impact on the tangential velocity distribution of FP as per its location in the FP slipstream (Fig. 10(b3)). The tangential velocity distribution of FP in CRAP on Plane C shows seven distinct change cycles corresponding to the total number of FP and RP blades.

### 3.3 Hydrodynamic performance analysis of RP

Fig. 16 shows the geometries of RP alone and RP+PU. The front end of the RP hub is closed in the RP alone configuration, and the hub of FP is included to close the geometry of RP+PU. Fig. 17 shows the corresponding computational meshes of RP+PU and RP alone used for simulations. The hydrodynamic performances of RP alone and RP+PU at various advance coefficients are simulated, and the results are analyzed in combination with the results of RP in CRAP. As RP is located downstream of PU, the effect of PU on the trailing vortex structure of RP can be neglected. Therefore, the trailing vortex structures of RP alone and RP in RP+PU naturally extend backward, as is the case for FP alone. The effect of FP on the trailing vortex structure of RP can be thoroughly analyzed by Figs. 10(a3)-(c3). The trailing vortex structures of RP alone, RP+PU, and CRAP are not presented in this subsection.

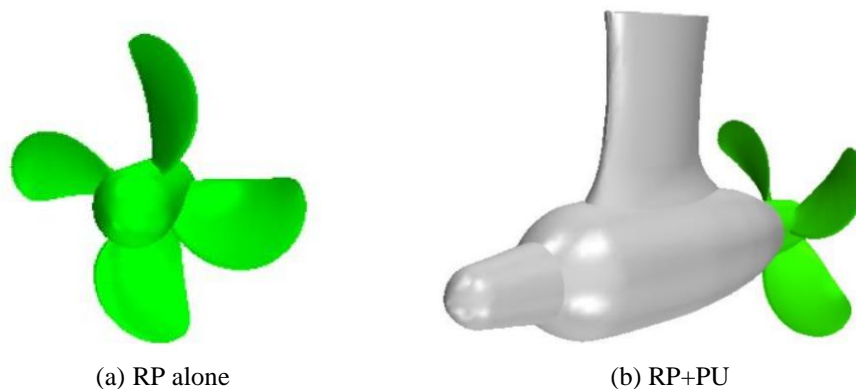


**Fig. 16** Geometries used for RP analysis

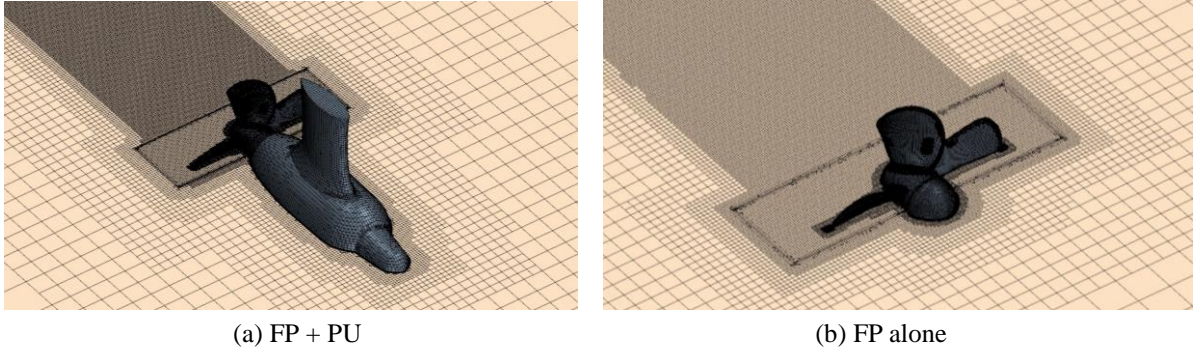
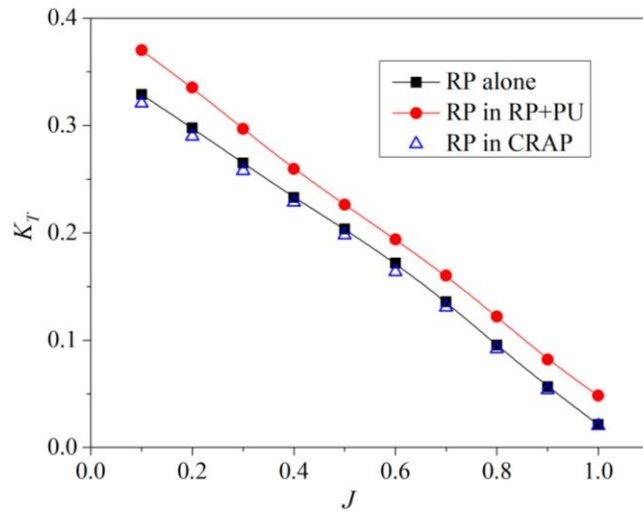
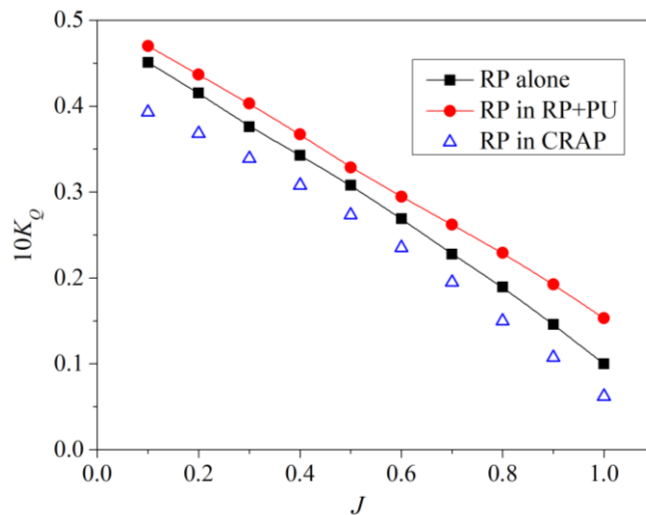


**Fig. 17** Computational meshes for FP + PU and FP alone



(a) Thrusts



(b) Torques

**Fig. 18** Time-averaged thrusts and torques of RP in three different configurations

Fig. 18 shows the time-averaged hydrodynamic forces (thrusts and torques) of RP, over four revolutions under convergence condition, in three different configurations at various advance coefficients. Unlike FP, the hydrodynamic forces of RP vary considerably in three different configurations. The hydrodynamic forces of RP in RP+PU are obviously higher than those of RP alone, mainly due to the blockage effect of PU, which decreases the axial inflow velocity of RP to some extent. The effective attack angles increase as axial inflow velocity decreases. Thus, RP bears higher loads and experiences higher thrusts and torques than other parts of the system. Compared to the thrust of RP alone, the thrust increase of RP in RP+PU

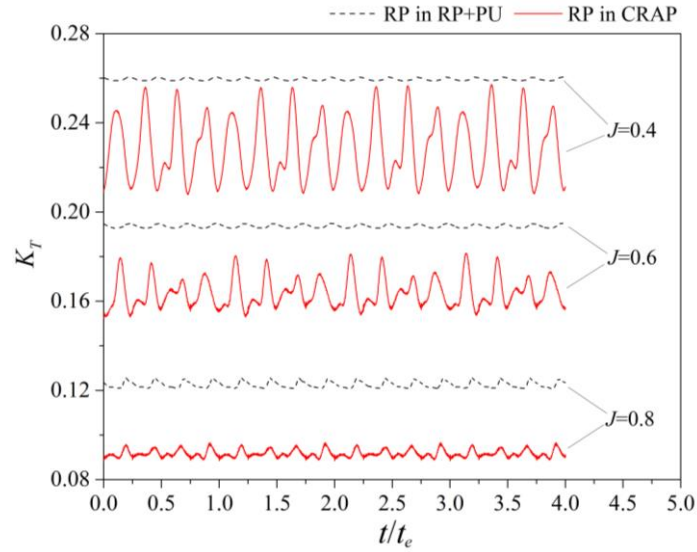
decreases with the increase of advance coefficient. In contrast, compared with the torque of RP alone, the torque increase of RP in RP+PU exhibits a reverse change trend. The propulsive efficiency of RP in RP+PU increases slightly compared with that of RP alone, though the increase is limited.

The hydrodynamic forces of RP in CRAP, especially the torque, are lower than those of RP in RP+PU. This is mainly because FP is located upstream of RP, and RP works in the FP slipstream (see Figs. 10(a3)-(c3)), so the RP inflow velocity is increased significantly. Thus RP bears smaller loads and has lower thrusts and torques. Under the joint influence of FP and PU, the thrusts of RP in CRAP are slightly lower than those of RP alone, while the torques of RP in CRAP are markedly lower than those of RP alone. The propulsive efficiency of RP in CRAP shows an increase of 17.3% on average compared with that of RP alone. The increase in propulsive efficiency of RP in CRAP is mainly attributed to FP, and PU mainly affects the values of the hydrodynamic forces of RP.

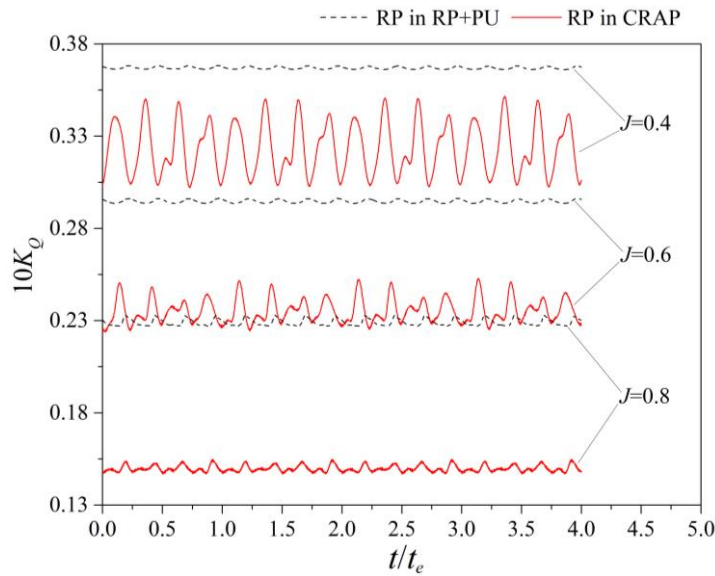
Fig. 19 gives the time histories of the hydrodynamic forces of RP in RP+PU and CRAP. The hydrodynamic forces of RP alone are not included in Fig. 19, as the motion of RP alone is steady and its hydrodynamic forces do not change over time. The hydrodynamic forces shown in Fig. 19 refer to the hydrodynamic forces of RP blades without those of the corresponding hub.

The hydrodynamic forces of RP in RP+PU fluctuate regularly in time domain at a frequency four times the shaft frequency. This is mainly because, as PU is at rest, the induced velocities of PU on the RP disc are equivalent to a non-uniform static wake field; additionally, RP has four blades each of which experiences the same changes in inflow. Regarding CRAP, the induced velocities of FP on the RP disc are equivalent to a transient wake field as the relative positions of FP and RP change over time. The effective wake field of RP is comprised of the static wake field of PU and the transient wake field of FP. Thus, the effective wake field of RP is transient and non-uniform, and the hydrodynamic forces of RP in CRAP fluctuate irregularly in time domain.

The blockage effect of PU intensifies as advance coefficient increases, so the static wake field of PU on the RP disc becomes increasingly non-uniform. The unsteady fluctuation amplitudes of the hydrodynamic forces of RP in RP+PU increase slightly as advance coefficient increases. In general, PU has rather small contribution to the unsteadiness of the hydrodynamic forces of RP, though it causes the hydrodynamic forces of RP to increase obviously in RP+PU compared to RP alone. At a low advance coefficient, the fluctuations of the hydrodynamic forces of RP are much stronger in CRAP than those in RP+PU. The unsteady fluctuation amplitudes of the hydrodynamic forces of RP in CRAP markedly decrease as the advance coefficient increases, and the difference between the fluctuation amplitudes of the hydrodynamic forces of RP in CRAP and those in RP+PU decreases with the increase of advance coefficient. For the CRAP studied in this work, the fluctuation amplitudes of the hydrodynamic forces of RP in CRAP are much closer to those in RP+PU at  $J=0.8$ . This means that the effect of FP on the unsteadiness of the hydrodynamic forces of RP is dominant under heavy loading conditions, and the unsteadiness is weakened under the joint effect of FP and PU under light loading conditions.



(a) Thrusts



(b) Torques

**Fig. 19** Hydrodynamic forces of RP in different configurations over four revolutions under convergence conditions

Fig. 20 shows the unsteady change trends of the hydrodynamic forces of the key blade of RP. The hydrodynamic forces of the key blade of RP in RP+PU change in a regular manner over time due to the existence of strut; the fluctuation amplitude increases as the advance coefficient increases. The key blade of RP in RP+PU has the maximum hydrodynamic forces when it rotates behind the strut, whereas the hydrodynamic forces are relatively stable at other angular positions. The fluctuation amplitudes of the hydrodynamic forces of the key blade of RP in CRAP decrease remarkably with the increase of advance coefficient. The key blade of RP in CRAP has the maximum hydrodynamic forces when it rotates to the right side of the strut, and has the minimum hydrodynamic forces when it rotates behind the strut due to the joint effect of FP and PU. At other angular positions, the hydrodynamic forces in CRAP exhibit moderate fluctuations. The difference in fluctuation amplitude between RP+PU and CRAP decreases with the increase of advance coefficient, and the fluctuation amplitudes are even slightly lower in CRAP than those in RP+PU at  $J=0.8$ .

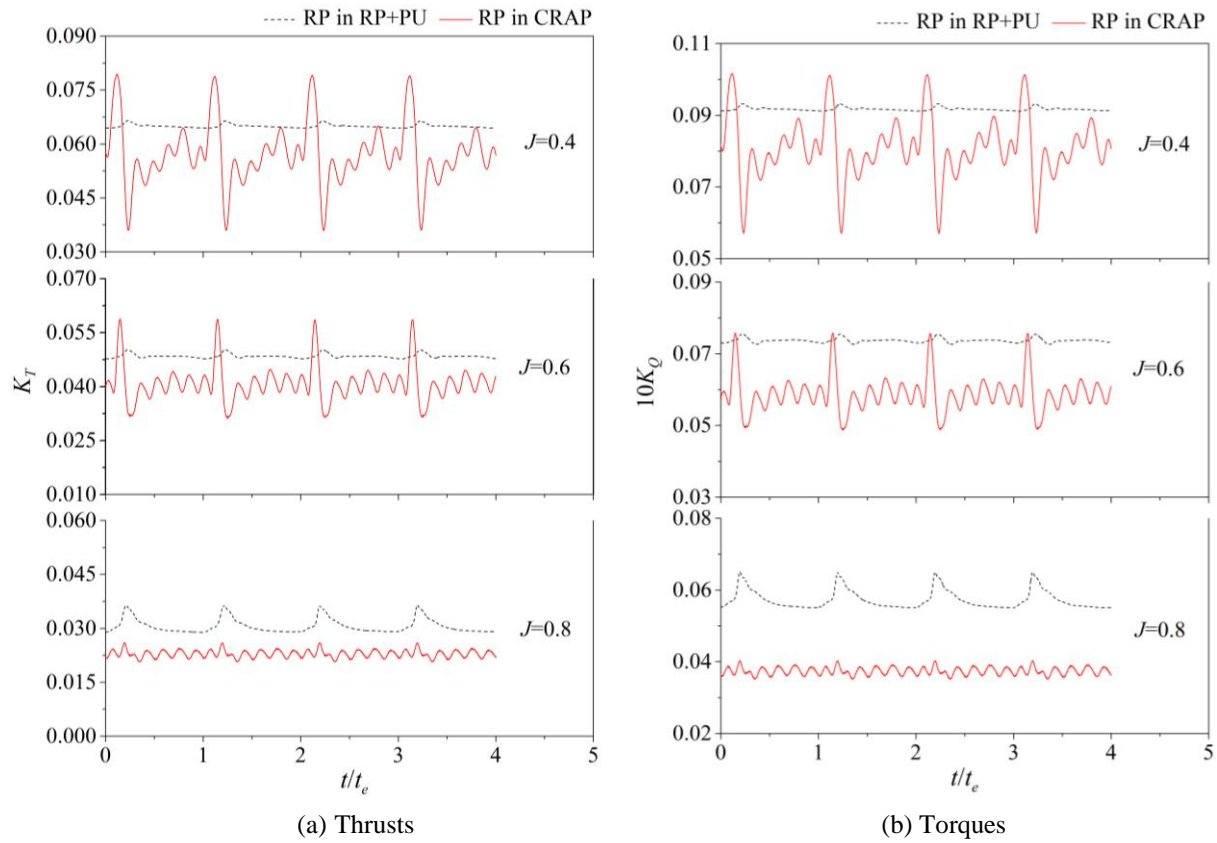


**Fig. 20** Hydrodynamic forces of the key blade of RP in different configurations over four revolutions under convergence conditions

Fig. 21 shows the velocity magnitude distributions of RP in the  $Y-\theta$  spread plane of 0.7R at  $J=0.4$  for different configurations,  $\theta$  is the angular position of the propeller blade. This radial plane shows the flow past specific blade sections. As RP is a left-handed propeller, the blade rotates from right to left in this plane, and the fluid flows from top to bottom. The relative location of each blade is revealed in this radial plane. In other word, it can also be regarded as the velocity magnitude distribution of a single blade at different angular position in one cycle. For RP in RP+PU, the region behind the strut shows lower velocity than other regions before RP in Fig. 21(b). The key blade produces higher hydrodynamic forces when it passes through this low velocity region, as given in Fig. 20. The flow field around RP in CRAP is much complicated under the combined action of FP with PU, as shown in Fig. 21(c). The strut wake region is deflective to the right side under the effect of FP, and this makes the key blade of RP produce the maximum hydrodynamic forces at the right side of the strut.

The hydrodynamic characteristics of RP and FP (Subsection 3.2) suggest that FP and PU have a significant effect on the hydrodynamic forces of RP and the corresponding unsteadiness. The effect of FP on the unsteadiness of the hydrodynamic forces of RP is dominant under heavy loading conditions, while the effect of PU gets more obvious under light loading conditions. The effect of PU on the hydrodynamic forces of FP and the corresponding unsteadiness is found to be dominant, and the effect of RP is found to be rather moderate.

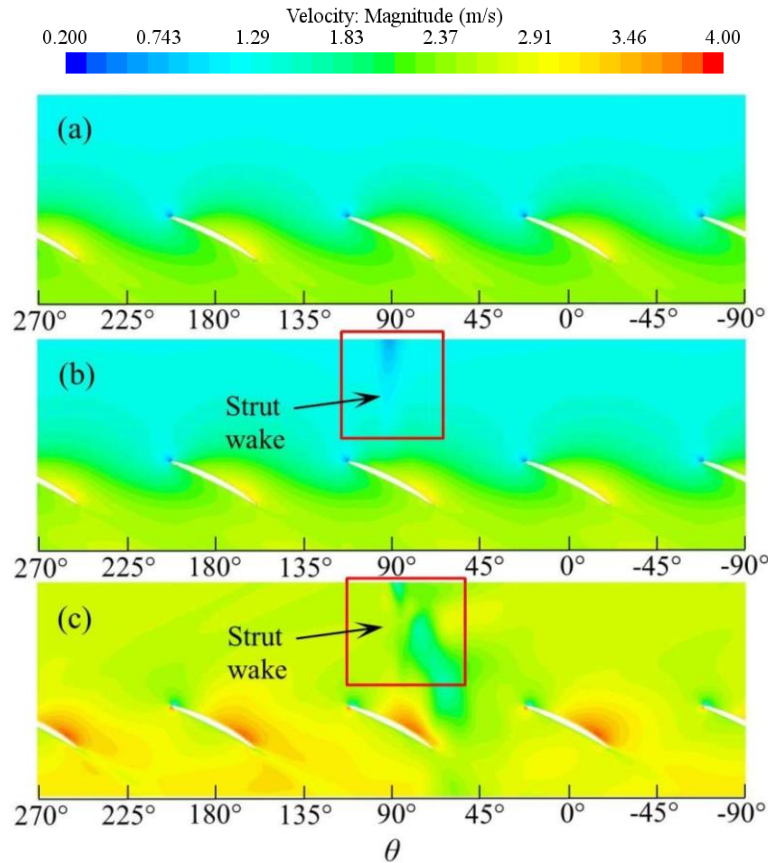


**Fig. 21** Velocity in the Y- $\theta$  spread plane of 0.7R at  $J=0.4$ . (a) RP alone; (b) RP in RP + PU; (c) RP in CRAP

### 3.4 Hydrodynamic performance analysis of PU

Fig. 22 shows the geometry of the PU component under analysis here. The hubs of FP and RP are included to close the geometry. The resistances of PU alone at various advance coefficients are simulated and the results are analyzed in combination to the FP+PU, RP+PU, and CRAP configurations.



**Fig. 22** Geometry used for PU analyses

The time-averaged resistances of PU, over four revolutions under convergence condition, in different configurations at various advance coefficients are shown in Fig. 23, where the resistances of the hubs of FP and RP are neglected. It can be known that the resistance of PU alone increases with the increase of advance coefficient, and the increasing rate increases gradually. The resistances of PU are significantly increased at different advance coefficients owing to the effects of FP and RP.

The resistance of PU in RP+PU exhibits a similar change trend as that of PU alone, and increases gradually with the increase of advance coefficient. The increasing rate of the resistance of PU in RP+PU decreases gradually. The resistance of PU in RP+PU can be divided into the open-water resistance and the induced resistance generated by RP. The open-water resistance is generated by the uniform inflow. The induced velocities of RP are mainly caused by the suction role, and are stronger on the PU afterbody than its forebody. According to the Bernoulli equation, the pressure distribution is inversely proportional to the inflow velocity. Therefore, RP induces lower pressure on the PU afterbody and increases the pressure difference between the PU afterbody and forebody.

As the suction role of RP abates with the increase of advance coefficient, the effect of RP on the resistance of PU is relatively weak under light loading conditions. PU is located in the slipstream of FP, which accelerates the flow around PU, and the induced velocities of FP on the PU afterbody are higher than those on the forebody. The effect of FP on the PU resistance is more obvious (see the results of PU in FP+PU) compared with RP. The PU resistance in FP+PU first increases and then decreases. The effect of FP on the PU resistance is more significant under heavy loading conditions. The resistance of PU in CRAP exhibits a similar change trend as that of PU in FP+PU. However, the resistances of PU in CRAP are slightly higher than those in FP+PU when  $J \leq 0.4$ , but lower when  $J > 0.4$  under the joint effect of FP and RP. This phenomenon is mainly attributed to the pressure drags of PU in FP+PU and CRAP, as shown in Fig. 24. The friction drags of PU in FP+PU and CRAP increase gradually with the increase of advance coefficient.

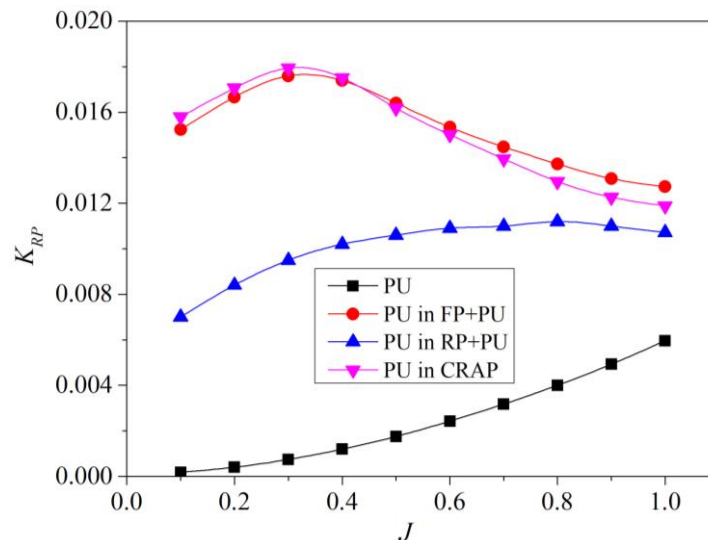


Fig. 23 Time-averaged resistance of PU in different configurations

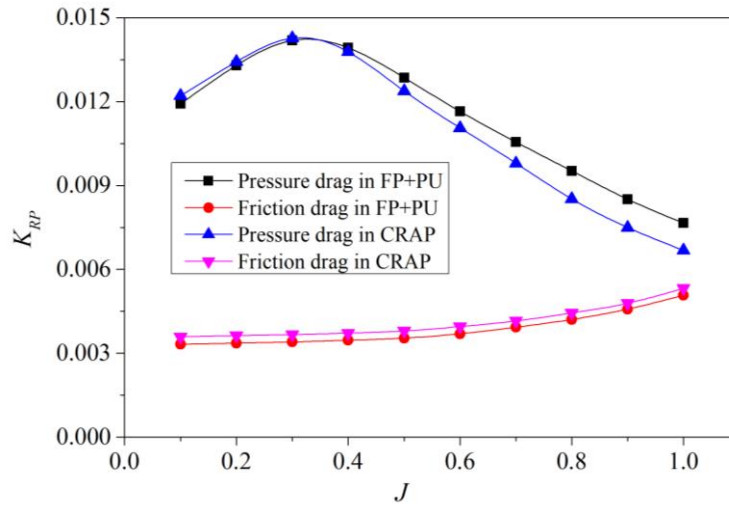


Fig. 24 Pressure and friction drags of PU in FP+PU and CRAP

To investigate the effects of FP and RP on the unsteady characteristics of the PU resistance, Fig. 25 presents the time histories of the PU resistance in different configurations at  $J=0.6$ . The PU resistances in FP+PU and RP+PU fluctuate regularly to some extent in each rotation period of propeller and the unsteady fluctuation amplitudes are stronger in FP+PU than those in RP+PU. Therefore, FP exerts a more intense effect on the unsteadiness of the PU resistance than RP. Under the combined action of FP and RP, the PU resistance in CRAP fluctuates irregularly in each rotation period of propeller and the fluctuation amplitude increases dramatically compared with those in FP+PU and RP+PU.

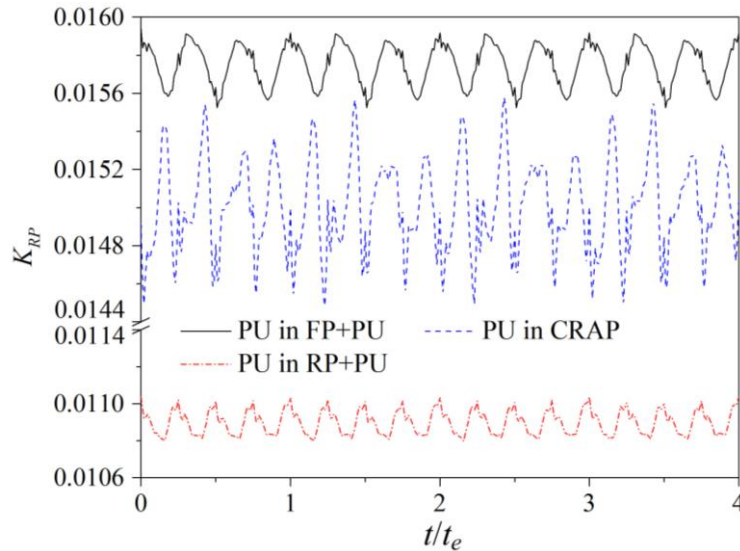


Fig. 25 Time histories of PU resistance in different configurations over four revolutions under convergence conditions at  $J=0.6$

#### 4. Conclusions

In this study, numerical simulations of the hydrodynamic performance of CRAP are carried out, and the hydrodynamic coupling characteristics among FP, RP, and PU are investigated in depth. The conclusions of this study can be summarized as follows.

The numerical method is validated based on a puller-type podded propeller. Grid sensitivity analysis reveals that the uncertainty values of the hydrodynamic forces under different inflow conditions are relatively small. The hydrodynamic forces of the puller-typed

podded propeller as observed on a basic grid are in close accordance with the experimental data at various advance coefficients. To strike a balance between computational cost and accuracy, the basic grid strategy is used for further numerical simulations of CRAP.

The hydrodynamic performance of CRAP is quantitatively analyzed based on FP, RP and PU, respectively. PU markedly affects the values and unsteadiness of the hydrodynamic forces of FP, while RP exerts no such effect. The fluctuating amplitudes of the thrusts and torques of FP increase with the increase of advance coefficient. PU is found to have a similar effect on the hydrodynamic forces of RP. FP has an obvious effect on the hydrodynamic forces of RP, as RP is located in the slipstream of FP. The hydrodynamic forces of RP fluctuate irregularly in time domain under the joint effect of FP and PU, and their fluctuating amplitudes decrease with the increase of advance coefficient. The effect of FP on the unsteadiness of the hydrodynamic forces of RP is dominant under heavy loading conditions, while the unsteadiness is weakened under the joint effect of FP and PU under light loading conditions. In general, PU is found to exert basically the same effect on the hydrodynamic performances of FP and RP. RP has a weak effect on the hydrodynamic performance of FP, while FP intensely affects that of RP.

Both FP and RP are found to have a significant effect on the PU resistance. The time-averaged resistances of PU in FP+PU exhibit the same change trends as that in CRAP, and the differences are small. Therefore, the effect of FP on the resistance of PU is more remarkable compared with that of RP. The resistance of PU fluctuates regularly under the effect of only the FP or RP, but shows remarkable irregularity and higher fluctuation amplitude under the combined action of FP and RP.

The unsteady characteristics of CRAP are found to be dominated by RP, especially at low advance coefficients. Therefore, RP is the main source of noise and fluctuating pressure of CRAPs. The hydrodynamic performance of CRAP can be improved via an optimization design based on the hydrodynamic coupling characteristics among FP, RP, and PU. The results of this work can provide a technical reference for CRAP design, as well as for cavitation and noise studies on CRAPs.

## Acknowledgement

This research is financially supported by the Liaoning Provincial Natural Science Foundation of China (Grant No. 2019ZD0161) and the Project funded by China Postdoctoral Science Foundation (Grant No. 2020M680935).

## REFERENCES

- [1] Jukola, H., Ronkainen, T., 2006. Contra-rotating propellers - combination of DP capability, fuel economy and environment. *Proceedings of the Dynamic Positioning Conference*.
- [2] Hou, L.X., Hu, A.K., 2018. Numerical design of contra-rotating azimuth propulsor using vortex theory coupled with panel method. *Ocean Engineering*, 156, 512-522. <https://doi.org/10.1016/j.oceaneng.2018.03.026>
- [3] Hou, L.X., Hu, A.K., Wang, S., 2019. Energy saving performance analysis of contra-rotating azimuth propulsor. Part 2: Optimal matching investigation in model scale. *Applied Ocean Research*, 88, 29-36. <https://doi.org/10.1016/j.apor.2019.04.016>
- [4] Su, Y., Kinnas, S.A., Jukola, H., 2017. Application of a BEM/RANS interactive method to contra-rotating propellers. *Proceedings of the Fifth International Symposium on Marine Propulsion*, Espoo, Finland.

- [5] Boucetta, D., Imine, O., 2019. Numerical simulation of the cavitating flow around marine co-rotating tandem propellers. *Brodogradnja*, 73(1), 43-57. <https://doi.org/10.21278/brod70104>
- [6] Dai, K., Li, Y.B., Gong, J.Y., Fu, Z., Li, A., Zhang, D.P., 2022. Numerical study on propulsive factors in regular head and oblique waves. *Brodogradnja*, 73(1), 37-56. <https://doi.org/10.21278/brod73103>
- [7] Balaras, E., Schroeder, S., Posa, A., 2015. Large-eddy simulations of submarine propellers. *Journal of Ship Research*, 59, 227-237. <https://doi.org/10.5957/jsr.2015.59.4.227>
- [8] Kumar, P., Mahesh, K., 2017. Large eddy simulation of propeller wake instabilities. *Journal of Fluid Mechanics*, 814, 361-396. <https://doi.org/10.1017/jfm.2017.20>
- [9] Posa, A., Broglio, R., Felli, M., Falchi, M., Balaras, E., 2019. Characterization of the wake of a submarine propeller via large-Eddy simulation. *Computers & Fluids*, 184, 138-152. <https://doi.org/10.1016/j.compfluid.2019.03.011>
- [10] Heydari, M., Sadat-Hosseini, H., 2020. Analysis of propeller wake field and vortical structures using k- $\omega$  SST method. *Ocean Engineering*, 204, 107247. <https://doi.org/10.1016/j.oceaneng.2020.107247>
- [11] Spalart, P.R., 2009. Detached-eddy simulation. *Annual Review of Fluid Mechanics*, 41, 181-202. <https://doi.org/10.1146/annurev.fluid.010908.165130>
- [12] Chase, N., Carrica, P.M., 2013. Submarine propeller computations and application to self-propulsion of DARPA Suboff. *Ocean Engineering*, 60, 68-80. <https://doi.org/10.1016/j.oceaneng.2012.12.029>
- [13] Degiuli, N., Farkas, A., Martic, I., Zeman, I., Ruggiero, V., Vasiljevic, V., 2021. Numerical and experimental assessment of the total resistance of yacht. *Brodogradnja*, 72(3), 61-80. <https://doi.org/10.21278/brod72305>
- [14] Carrica, P.M., Fu, H., Stern, F., 2011. Computations of self-propulsion free to sink and trim and of motions in head waves of the KRISO container ship (KCS) model. *Applied Ocean Research*, 33, 309-320. <https://doi.org/10.1016/j.apor.2011.07.003>
- [15] Di Mascio, A., Muscari, R., Dubbioso, G., 2014. On the wake dynamics of a propeller operating in drift. *Journal of Fluid Mechanics*, 754, 263-307. <https://doi.org/10.1017/jfm.2014.390>
- [16] Gong, J., Guo, C.Y., Zhao, D.G., Wu, T.C., Song, K.W., 2018. A comparative DES study of wake vortex evolution for ducted and non-ducted propellers. *Ocean Engineering*, 160, 78-93. <https://doi.org/10.1016/j.oceaneng.2018.04.054>
- [17] Lungu, A., 2020. A DES-SST based assessment of hydrodynamic performances of the wetted and cavitating PPTC propeller. *Journal of Marine Science and Engineering*, 8(4), 297. <https://doi.org/10.3390/jmse8040297>
- [18] Sun, S., Wang, C., Guo, C., Zhang, Y., Sun, C., Liu, P., 2020. Numerical study of scale effect on the wake dynamics of a propeller. *Ocean Engineering*, 196, 106810.1-106810.14. <https://doi.org/10.1016/j.oceaneng.2019.106810>
- [19] Zhang, Y.X., Wu, X.P., Zhou, Z.Y., Cheng, X.K., Li, Y.L., 2019. A numerical study on the interaction between forward and aft propellers of hybrid CRP pod propulsion systems. *Ocean Engineering*, 186, 106084. <https://doi.org/10.1016/j.oceaneng.2019.05.066>
- [20] Hu, J., Ning, X.S., Zhao, W., Li, F.G., Ma, J.C., Zhang, W.P., Sun, S.L., Zou, M.S., Lin, C.G., 2021. Numerical simulation of the cavitating noise of contra-rotating propellers based on detached eddy simulation and the Ffowcs Williams–Hawkings acoustics equation. *Physics of Fluids*, 22, 115117. <https://doi.org/10.1063/5.0065456>
- [21] Sanders, L., Mincu, D.C., Vitagliano, Minervino, M., Kennedy, J., Bennett, G., 2017. Prediction of the lkAeroacoustics, 16(7-8), 626-648. <https://doi.org/10.1177/1475472X17734334>
- [22] Smith, D.A., 2020. Aerodynamic and Aeroacoustic Analysis of Counter Rotating Open Rotors. School of Engineering Department of Mechanic Aerospace and Civil Engineering, University of Manchester.
- [23] Liu, P., 2006. The design of a podded propeller base model geometry and prediction of its hydrodynamics. Technical Report no: TR-2006-16, Institute for Ocean Technology, National Research Council Canada (IOT-NRC).
- [24] Gaggero, S., Tani, G., Viviani, M., Conti, F., 2014. A study on the numerical prediction of propellers cavitating tip vortex. *Ocean Engineering*, 92, 137-161. <https://doi.org/10.1016/j.oceaneng.2014.09.042>
- [25] Jang Y.H., Eom, M.J., Paik, K.J., Kim, S.H., Song, G., 2020. A numerical study on the open water performance of a propeller with sinusoidal pitch motion. *Brodogradnja*, 71(1), 71-83. <https://doi.org/10.21278/brod71105>
- [26] Roache, P.J., 1997. Quantification of uncertainty in computational fluid dynamics. *Annual Review of Fluid Mechanics*, 29, 123-160. <https://doi.org/10.1146/annurev.fluid.29.1.123>

- [27] Dai, K., Li, Y.B., 2021. Experimental and numerical investigation on maneuvering performance of small waterplane area twin hull. *Brodogradnja*, 72(2), 93-114. <https://doi.org/10.21278/brod72206>
- [28] Muscari, R., Di Mascio, A., Verzicco, R., 2013. Modeling of vortex dynamics in the wake of a marine propeller. *Computers & Fluids*, 73, 65-79. <https://doi.org/10.1016/j.compfluid.2012.12.003>
- [29] Liu, P.; Islam, M.; Veitch, B., 2009. Unsteady hydromechanics of a steering podded propeller unit. *Ocean Engineering*, 36, 1003-1014. <https://doi.org/10.1016/j.oceaneng.2009.05.012>
- [30] Jeong, J., Hussain, F., 1995. On the identification of a vortex. *Journal of Fluid Mechanics*, 285, 69-94. <https://doi.org/10.1017/S0022112095000462>

Submitted: 18.07.2022. Hou Lixun, houlixun@dlmu.edu.cn  
Wang Qingcai  
Accepted: 24.10.2022. Dalian Maritime University, School of Naval Architecture and Ocean  
Engineering